Research Article

Jie Liu, Fatemeh Movahedi, Bing Sun, Luyao Sun, Bing Zhang, Jingjing Wang, Li Li and Zhi Ping Xu*

Immunostimulatory photochemotherapeutic nanocapsule for enhanced colon cancer treatment

https://doi.org/10.1515/nanoph-2021-0202
Received April 30, 2021; accepted June 29, 2021; published online July 22, 2021

Abstract: Immunotherapy has made great progress in recent years while most cancer patients cannot benefit from it. Photochemotherapy combination strategy holds great promise for developing novel immunotherapy for the patients bearing immunosuppressive tumors such as colon cancer. In this research, a novel core/shell-structured polydopamine (PDA)-based nanoplatform is constructed to load two Food and Drug Administration (FDA)-approved cytotoxic drugs, i.e. immunostimulatory doxorubicin (Dox) and immunomodulatory curcumin (Cur) to achieve immunostimulatory photochemotherapy of primary colon tumors upon 808 nm near infrared (NIR) irradiation (1 W/cm^2 for 5 min) and subsequent prevention of rechallenged distant colon tumors. The experimental data have shown that PDA-mediated photothermal therapy (PTT) synergized two therapeutic drugs in inducing colon cancer cell death and very efficiently inhibited the primary tumor growth (by ~92%) at very low doses of therapeutics (0.25, 5, and 30 mg/kg of Dox, Cur, and PDA, respectively). More significantly, the combined photochemotherapy promoted strong adaptive antitumor immune responses and successfully prevented tumorigenesis in the setting of tumor rechallenge model. Our research has thus demonstrated the promising efficacy of this photochemotherapeutic nanoformulation for colon cancer treatment and provided a way to improve immunostimulatory effects of conventional chemotherapeutic drugs.

***Corresponding author: Zhi Ping Xu**, Australian Institute for Bioengineering and Nanotechnology, the University of Queensland, St Lucia 4072, QLD, Australia, E-mail: gordonxu@uq.edu.au. https://orcid.org/0000-0001-6070-5035
Jie Liu, Fatemeh Movahedi, Bing Sun, Luyao Sun, Bing Zhang, Jingjing Wang and Li Li, Australian Institute for Bioengineering and Nanotechnology, the University of Queensland, St Lucia 4072, QLD, Australia. https://orcid.org/0000-0002-5796-8181 (J. Liu)

Keywords: curcumin; doxorubicin; immunostimulatory nanomedicine; photochemotherapy of colon cancer; polydopamine.

1 Introduction

Immunotherapy has revolutionized the field of metastatic cancer therapy via targeting immunosuppressive checkpoint molecules [1]. However, only about 12.5% of the patients receiving immunotherapy in 2018 would benefit and particularly some colon cancer patients did not even respond to immunotherapy [2]. Nowadays, the therapeutic efficacy of conventional chemotherapy is known to involve a considerable immunological component and three chemo-immunotherapeutic combinations have been already approved by FDA and European Medicines Agency (EMA) for their clinical outperformance [2]. Therefore, the chemo-immunotherapeutic combination strategy has shown the promise to benefit such cancer patients who have poor responsiveness to the current immunotherapy.

Dox, as a confirmed immunogenic agent, shows immunostimulatory effects on tumor cells via immunogenic cell death (ICD), which drives tumor cells to release adjuvant-like damage-associated molecule patterns (DAMPs) and tumor associated antigens (TAAs) for innate immune cells to prime adaptive immune responses [3]. Moreover, Dox can deplete immunosuppressive cells and favor immune effector cells to some certain extent [2]. Nonetheless, it is very challenging to harness its immunostimulatory advantages. For example, tumor cells would impede these immunogenic effects by circumventing ICD via acquired treatment resistance [4]. Besides, reactive oxygen species (ROS)-rich tumor microenvironment (TME) would damage DAMPs, in particular, high mobility group box 1(HMGB1), and then their adjuvanticity would be dampened accordingly [5]. In addition, the bone marrow suppression effect of Dox undermines its potential of stimulating immune effector cells [2]. As such, the full potential of Dox in stimulating immunotherapy remains not to be well achieved.

Antioxidant Cur, as a well-known inhibitor of the janus kinase (JAK)-signal transducer and activator of transcription (STAT) pathway [6, 7], has attracted increasing research interests due to its potential to complementarily enhance the immunostimulatory activity of immunogenic chemotherapy. The major advantage of Cur is its ability of depleting immunosuppressive cells via JAK-STAT pathway [7]. Moreover, Cur has been found to enhance immunogenicity of Dox chemotherapy via causing endoplasmic reticulum (ER) stress [8]. Its antioxidant property would also protect DAMPs from oxidation by ROS in TME and attenuate the bone marrow suppression effect of Dox. Therefore, Cur would complementarily enhance the immunostimulatory activity of Dox, while the challenges for Cur application include its instability in aqueous media, high hydrophobicity and low bioavailability [9].

Nanomaterials offer the possibility to strengthen the immunostimulatory effects of chemotherapeutics owing to the synergetic actions [10]. Recently, PTT has been intensely investigated in combination with chemotherapy to enhance the immunogenic capability [11–13]. PDA is a biocompatible material and can be readily developed as functional delivery systems for hydrophobic anticancer agents such as Dox and Cur. Moreover, PDA is a well-known photothermal material with a high photothermal conversion efficiency (40%) [14]. Therefore, PDA nanomaterials are promising in combination with Dox and Cur to explore a novel immunostimulatory photochemotherapeutic nanomedicine.

Therefore, a core/shell-structured multifunctional PDA nanoplatform has been constructed by encapsulating Dox and Cur (DCP-F, Scheme 1(a)) in order to orchestrate the immunostimulatory effects of Dox and Cur in combination with PTT. In this system, immunostimulatory Cur and Dox are precipitated and encapsulated by dopamine (DA) polymerization (Step 1 and 2 in Scheme 1(a)), followed by folic acid (FA) conjugation (Step 3 in Scheme 1(a)) for targeted delivery. As schematically outlined in Scheme 1(b), PDA-mediated PTT together with the responsive release of Dox and Cur may collectively induce cancer cell apoptosis and enhance ICD in a synergic manner, releasing abundant DAMPs and TAAs into TME and engaging pattern recognition receptors (PRRs) to stimulate innate immune responses, e.g. dendritic cell (DC) maturation and interferon (IFN) secretion, and adaptive immune responses involving $CD8^+$ T effector cells and IgG production. Note that antioxidant Cur would also modulate host redox homeostasis, inflammation and immune responses against tumor, such as specifically dampening immunosuppressive T regulatory cells (T_{reg}) in peripheral immune organs and TME via the JAK-STAT pathway [6, 7, 15], and mitigating the ROS level via its phenolic hydroxyl [9] together with PDA via direct depletion of oxidant species [16–18].

Thus, this research aimed to (1) develop a suitable approach to prepare such a multifunctional DCP-F nanoplatform in a control way; (2) determine the synergistic effect of PTT/Dox/Cur on induction of colon cancer cell (CT26) death; (3) evaluate the high inhibition to the primary tumor growth; and (4) validate the promotion of anticancer immunity and the efficient inhibition of distant tumor growth. The current research has demonstrated that DCP-F nanoparticles (NPs) successfully enhanced the photo-chemo-immunotherapy and established satisfactory immunity against primary and distal tumors. This work has provided an insight into enhancing immunostimulatory effects of conventional chemotherapeutic drugs in combination with PTT treatment via the PDA nanoplatform.

2 Materials and experiments

2.1 Materials and instruments

All chemicals were purchased from Sigma-Aldrich (St Louis, MO) if not specially mentioned. Dox was purchased from Pfizer Ltd. Phospholipids (1,2-dioleoyl-sn-glycero-3-phosphate, DOPA) was purchased from Avanti Polar Lipids, Inc. Fetal Bovine Serum (FBS), penicillin/streptomycin antibiotics (P/S), and cell culture medium were purchased from Gibco™ Thermo Fisher Scientific Inc. Fluorescent antibodies from BioLegend, Inc., including TruStain FcX™ (Cat#101319), PerCP/Cyanine5.5-CD8a (100733), CD3-Brilliant Violet 421(Cat#100227) and CD4-PE (Cat#100408), and fluorescent secondary antibody Goat Anti-Mouse IgG H&L (Cat#ab150115) from Abcam PLC were used for cell staining and flow cytometry. Deionized water (DI H_2O) used in experiments was Milli-Q water (Ω = 18.2 at ambient temperature).

Transmission electron microscope (TEM; JEM-3010, ZEOL, Tokyo, Japan), Malvern NanoSizer (Malvern, UK), Fourier transform infrared spectroscopy (FTIR; Nicolet 6700, Thermo Scientific), and fluorescence microplate reader (Biotek, Winooski, VT) were used for material characterization. Dry bath incubator (EL01, Major science, Taiwan) and benchtop incubator shaker (New Brunswick™ Innova® 40/40R Shakers, Eppendorf AG) were used for incubation. Flow cytometry (Accuri C6 flow cytometer, BD Biosciences) was used to collect and analyze cytometry data. NIR irradiation was conducted using LEOPTICS® laser (Model: LE-LS-IR; Leo Photonics, Shenzhen, China).

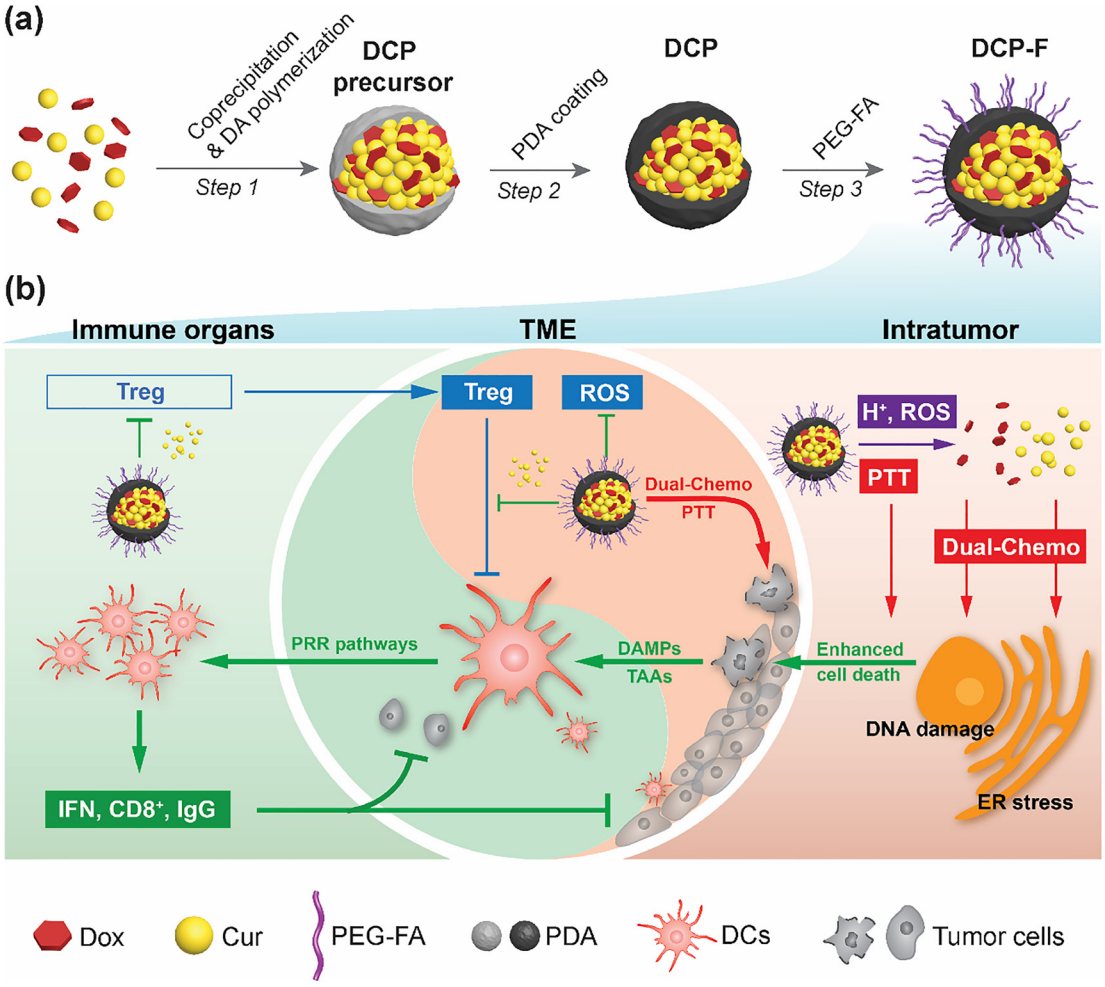

Scheme 1: The schematic of (a) preparation and (b) anticancer actions of DCP-F nanoparticles.

Thermal imaging and temperature monitoring were conducted using FLIRONE®PRO camera (P/N#435-0006-01) and analyzed using FLIR® Thermography Software. Light microscope (Olympus BX61) was used for imaging of hematoxylin and eosin (H&E)-stained tissue samples. The nanoparticle size in TEM images was estimated using Nano Measure software (V1.2.5, Jie Xu, Fudan University), and the mean size was calculated by counting all NPs in the TEM image. DNA gel electrophoresis images were recorded in Bio-Rad imaging system (ChemiDoc XRS+) and analyzed using ImageJ.

2.2 Preparation of DCP-F NPs

The DCP-F NPs were prepared in three steps, i.e. (1) encapsulating Dox/Cur into PDA capsules (Step 1 in Scheme 1(a)); (2) additional PDA coating (Step 2 in Scheme 1(a)); and (3) FA modification (Step 3 in Scheme 1(a)).

In Step 1, instant Dox/Cur self-aggregation was followed by local DA polymerization to make the DCP-F NP precursor. Typically, to coencapsulate Cur and Dox, 5 mL of solution (A) containing 1000 μg of DA was prepared and adjusted to pH 8.0 using 3% ammonia. Once solution A turned slightly brown in about 5 min, 0.5 mL of ethanol solution (B) containing Cur (800 μg) and Dox (0–100 μg) was stepwise added to solution A under mild magnetic stirring (120 rpm) for 24 h. To encapsulate Cur alone, 350 μL of solution B containing 700 μg Cur was mixed with the same volume of solution A to prepare CP-F NPs. In Step 2, additional DA was added to coat a shell as PDA on the NP surface. Briefly, the NP pellets were collected from the suspension prepared in Step 1 by centrifugation (20,000 g, 15 min) and then resuspended in DA solution (0.8 mg/mL of DA, pH 8.0 adjusted by 3% ammonia, 5 mL) under mild stirring (120 rpm) for 12 h. In Step 3, FA was grafted on the NP surface using house-made NH_2-PEG-FA conjugates via Schiff/Michael reaction between the amine group in NH_2-

PEG-FA and the catechol/quinine groups on the PDA shell. The NH_2-PEG-FA conjugates were preprepared via EDC/NHS chemistry in MES buffer (50 mM, pH 6.0) at the mass ratio of diamine PEG:FA:EDC:NHS of 2:1:1:1 under moderate stirring (500 rpm) for 24 h. Then, resulting NH_2-PEG-FA solution (100 μL) was added into the suspension prepared in Step 2 (pH 8.0 adjusted by 1 M NaOH, 2 mL) under moderate stirring for 2 h. As-prepared NPs were collected by centrifugation (20,000 g, 15 min) and redispersed in DI H_2O for further use.

Particularly, to make Dox-encapsulated DP-F NPs, PDA NPs (1000 μg) were prepared as reported [19] and mixed with Dox (20 μg) in DI H_2O (1 mL) for 24 h under moderate stirring (500 rpm), as done in Step 1. Then, 0.5 mL of the resulting NP suspension was collected and treated in the same protocol as in the next two steps.

2.3 Quantifying Cur and Dox in NPs

To quantify the Cur content in DCP-F and CP-F, the collected NP pellet from 200 μL of the suspension was completely dissolved in dimethyl sulfoxide (DMSO) (200 μL) for 2 h, and further diluted 5-fold using DMSO. The absorbance of Cur at 433 nm was used to calculate the Cur content according to its calibration curve in DMSO.

To quantify the Dox content in DCP-F, the collected pellet was dissolved in DMSO and then diluted 10-fold using HCl for 4 h. The fluorescence of Dox (F_{Dox}) at 595 nm upon excitation at 490 nm was used to calculate the Dox content according to its calibration curve (f) in HCl containing 10% DMSO (v/v):

$$\mathrm{Dox} = f\left(F_{\mathrm{Dox}} - F_{\mathrm{bg}}\right).$$

Note that the fluorescence of Cur was almost completely quenched in HCl aqueous solution and used as the background (F_{bg}). In particular, the Dox content in DP-F was measured as follows. The supernatant obtained in Step 1 was adjusted to pH 2.0 using HCl, the fluorescence of Dox in the supernatant was used to calculate the unloaded Dox, so that the Dox loading amount in NPs was estimated.

2.4 Drug release and PDA degradation

To profile pH-responsive Dox release, DCP-F NPs (1 mL, equivalent Dox at 6 μg/mL) was mixed with buffers (pH 7.4 and 5.0, respectively, 9 mL). Then, the suspension was incubated at 37 °C under shaking for 3, 6, 12, 24, 36, 48, and 72 h, respectively. At each time point, the supernatant (100 μL) was collected from 300 μL of aliquot by centrifugation (20,000 g, 5 min) for Dox florescence detection. After each measurement, the withdrawn aliquot and pellet were returned to the suspension as soon as possible. To profile the NIR-responsive Dox release, the DCP-F suspension (0.5 mL, pH 5.0, equivalent Dox at 6 μg/mL) in a cuvette at room temperature was irradiated with NIR laser (808 nm, 1 W/cm^2) for 8 min at a time interval of 1 h. At each time point, the supernatant (100 μL) was collected from the NP suspension by centrifugation (20,000 g, 5 min) for Dox florescence detection and release amount determination. After each measurement, the NP mixture was resuspended with the withdrawn supernatant as soon as possible for the next measurement. The accumulative amount of the released Dox was calculated as follows,

$$\mathrm{Dox}\,(\%) = W_t/W_0 \times 100\%$$

where W_t and W_0 are the Dox amount released at time t and the total Dox amount in DCP-F NPs, respectively.

To profile Cur release in the presence of phospholipid DOPA, DCP-F NPs (1 mL, equivalent Cur at 10 μg/mL) was mixed with buffers (pH 7.4 and 5.0, respectively, 4 mL). Then, the suspension was incubated at 37 °C under shaking for 12, 24, 48, and 72 h, respectively. At each time point, DCP-F NPs of 500 μL aliquot were collected by centrifugation (20,000 g, 15 min) for Cur detection as Section 2.3. The accumulative amount of the released Cur was calculated as follows;

$$\mathrm{Cur}\,(\%) = (W_0 - W_t)/W_0 \times 100\%$$

where W_t and W_0 are the residual Cur amount in DCP-F NPs at time t and the total Cur amount in DCP-F NPs, respectively.

To investigate PDA degradation in response to H_2O_2, DCP-F NPs (100 μg/mL of PDA) was treated with H_2O_2 (10 mM) at 37 °C in buffers at pH 5.0 and 7.4, respectively, for 3, 6, 12, 24, 36, and 48 h. The equivalent PDA in PBS (pH 7.4) was used as control. At each time point, 100 μL of suspension was taken to detect the absorption at 650 nm and the left PDA amount (W_t) was estimated according to the PDA calibration curve in buffers. Similarly, the accumulative amount of the degraded PDA was calculated as follows,

$$\mathrm{PDA}\,(\%) = (W_0 - W_t)/W_0 \times 100\%,$$

where W_0 is the total amount of PDA in DCP-F NPs.

2.5 Cellular uptake and *in vitro* anticancer efficacy

To investigate cellular uptake, CT26 cells were seeded in a 12-well plate at a density of 1×10^5 cells per well and

incubated at 37 °C under 5% CO_2 overnight until 90% confluence. Then, culture medium was replaced with 500 μL of fresh DMEM (10% PBS, 1% P/S) containing free Cur, and CP NPs, and CP-F NPs, respectively, at the equivalent Cur concentration of 20 μg/mL for 6 h incubation. After washing with PBS three times, the cells were lysed with 200 μL of TE lysis buffer (10 mM Tris, 5 mM EDTA, 0.2% Trition-100, pH 7.4), followed by five cycles of freezing and thawing processes. The cell suspension was then well mixed with DMSO (1.8 mL) for 2 h. The fluorescence intensity of free Cur in this DMSO-treated cell suspension was detected at 542 nm upon excitation at 433 nm. The Cur quantification was determined by the standard calibration curve of Cur in cell lysis containing 90% DMSO (v/v). The total protein amount in the cell lysis was determined by a BCA Protein Assay Kit (Thermal Scientific, Product No. 23225) as the internal standard. The cellular uptake of Cur was described as the mass ratio of Cur to the total proteins from the lysed cells. For FA competition assay, CT26 cells were first treated for 1 h with DMEM (10% PBS, 1% P/S) containing FA at concentrations of 0.5 and 1.0 mg/mL. Then, CP-F NPs were added at the Cur concentration of 20 μg/mL in culture medium. After incubation for another 6 h, the cells were collected and treated similarly to quantify the Cur uptake amount by the cells.

Cell viability experiments were conducted in 96-well plates. Free Cur, free Dox, and all nanoformulations were freshly prepared in DMEM (10% PBS, 1% P/S). Typically, CT26 cells were seeded at the density of 4.0×10^3 cells per well and incubated overnight at 37 °C with 5% CO_2 until around 60% cell confluence. Culture medium was then replaced with 100 μL of fresh medium containing nanoformulations at the equivalent Dox concentration of 0.1–5.0 μg/mL, and/or the equivalent Cur concentration of 2.0–20.0 μg/mL. NIR irradiation (1 W/cm^2 for 8 min) was conducted after 24 h cellular uptake. The cell viability was determined after another 24 h (48 h in total) incubation using the standard MTT assay protocol. Typically, culture medium was replaced by 100 μL of MTT solution (0.5 mg/mL in blank DMEM medium) in each well, followed by incubating for 4 h in a cell incubator at 37 °C with 5% CO_2, and then MTT solution was removed and 100 μL of DMSO was added to dissolve the MTT formazan for 10 min. The absorbance at 570 nm was measured in a microplate reader (Biotek, Winooski, VT) to estimate the cell viability. Note that combination index (CI) of treatments was determined as follows:

$$CI = (PTT_{expt} \times CT_{expt}) / (PTT \,\&\, CT)_{expt},$$

where PTT_{expt} and CT_{expt} are the obtained cell viability upon the treatment of PTT and chemotherapy (CT), respectively, and $(PTT\&CT)_{expt}$ is denoted as the obtained cell viability of the combination in this work. $PTT_{expt} \times CT_{expt}$ is denoted as the estimated cell viability of the simply additive combination of PTT and CT. Briefly, CI = 0.8–1.2, additive effect; CI = 1.2–1.4, mild synergistic effect; CI = 1.4–1.6, moderate synergistic effect; CI > 1.6, strong synergistic effect.

The integrity of the plasma membrane was determined by propidium iodide (PI; Sigma) exclusion assay [20] with slight modification. Briefly, CT26 cells were seeded at the density of 5.0×10^4 cells per well in 24-well plates and incubated overnight at 37 °C with 5% CO_2 until around 60% cell confluence. Culture medium was then replaced with 400 μL of fresh medium containing nanoformulations. NIR irradiation (1 W/cm^2 for 0–15 min) was conducted after 24 h cellular uptake. After 24 h of the NIR treatment, cells were collected and stained with 20 μg/mL of PI for 30 min before flow cytometry assay. Culture medium after 48 h of incubation was collected for DNA gel electrophoresis (50 μL sample; 4% agarose, 60 V, 0.5 h).

2.6 ROS-scavenging activity of DCP-F

The ROS-scavenging ability of DCP-F NPs was evaluated by fluorescence using H_2DCFDA as the ROS dye. Briefly, CT26, Raw 264.7 (Mouse macrophage cells), LX-2 (Human liver stellate cells) and Hepa1-6 (Mouse hepatoma cells) were seeded at the density of 2.5×10^4 cells per well in a 48-well plate and incubated overnight at 37 °C with 5% CO_2 until 80% confluence. Culture medium was replaced by 200 μL of fresh medium containing free Cur, P-F or CP-F NPs at the equivalent Cur (20 μg/mL) and PDA (120 μg/mL) for 6 h incubation. Then, 200 μL of TE lysis buffer (10 mM Tris, 5 mM EDTA, 0.2% Triton-100, pH 7.4) was added for 2 h incubation at room temperature after washing the cells with PBS three times. After 2 min shaking, the fluorescence was detected at 525 nm upon excitation at 491 nm. The ROS level in untreated cells (PBS) was used as the control level.

2.7 In vivo photothermal conversion and antitumor efficacy

The tumor model was built by subcutaneous (s.c.) injection of 2×10^6 CT26 colon cancer cells suspended in 100 μL of saline on the flank of BALB/c female mouse. If not specially mentioned, all animal operations were executed in accordance with the protocols and animal ethics certificate (AIBN/224/18) approved by the Animal Ethics Committee, The University of Queensland.

Infrared thermal camera FLIR ONE PRO was used to monitor the tumor surface temperature. To determine the optimal timepoint after intravenous (i.v.) injection of nanoformulations for PTT treatment, the tumor surface temperature was measured during NIR irradiation at 1 W/cm^2 for 5 min at 12, 18, and 24 h post injection. To determine the optimal NIR laser density, the tumor temperature was also monitored at 18 h post injection under NIR irradiation at 0.5, 0.7, and 1 W/cm^2 for 5 min, respectively.

In vivo anti-tumor efficacy was examined by randomly assigning the colon tumor-bearing mice into five groups (5 mice/group) when the tumor size reached 50–100 mm^3. In tumor inhibition experiments, five groups of mice received 150 μL of formulations at day 0 and 3 via i.v. injection, including PBS + *L* (G1), DP-F + *L* (G2), CP-F + *L* (G3), DCP-F (G4), and DCP-F + *L* (G5), where *L* is donated as NIR laser irradiation (1 W/cm^2, 5 min) at 18 h post-injection. In tumor rechallenge experiments, two groups received 150 μL of formulations at day 0 and 3 via i.v. injection, i.e. PBS (G6) and DCP-F + *L* (G7). Distal tumor was inoculated on Day 11 by s.c. injecting 2×10^6 CT26 colon cancer cells suspended in 100 μL of saline on the other flank of mice in both groups. The applied equivalent dosage of PDA, Cur, and Dox was 30, 5, and/or 0.25 mg/kg, respectively, in all formulations. During the therapy, the body weight and the tumor volume were monitored every other day. The tumor volume (V) was estimated using $V = (L \times W \times W) \times 0.5$, where L is the longest dimension and W the shortest dimension. Of note, according to the 3R rules (replacement, reduction and refinement) of animal welfare and ethics, the minimal number of mice was used in this experiment. In addition, the targeting capacity of FA-conjugated spherical PDA NPs was well documented in comparison to nontargeting PDA NPs [21, 22].

2.8 Spleen lymphocyte, serum IgG, and histology evaluation

To analyze lymphocytes in spleen, spleen tissues were harvested at the end of experiments and homogenized following the standard protocol. The obtained spleen cells were stained with the antibody-fluorophore conjugates from BioLegend for CD3 and CD8, followed by flow cytometry analyses. To analyze the specific IgG content in serum, 100 μL of CT26 cells (2×10^6 cells; PBS with 1% BSA) were incubated with 10 μL of mouse serum collected from treated mice at room temperature for 2 h under shaking at 100 rpm. The cells were then collected and washed 2 times with PBS, followed by incubating with fluorescent secondary IgG antibody at room temperature for 2 h under shaking at 100 rpm. Then the cells were collected and washed 2 times with PBS for flow cytometry analysis. For NP safety evaluation, main organs were harvested and stained with H&E, followed by imaging in a light microscope.

2.9 Statistical analysis

Data are shown as the mean ± standard error of the mean (Mean ± SEM) or the mean ± standard deviation (Mean ± SD). The data were analyzed using the Student's *t*-test to compare the difference significance. ns, not significant, $p > 0.05$; *$p < 0.05$; **$p < 0.01$; ***$p < 0.001$.

3 Result and discussion

3.1 Characteristics of DCP-F NPs with high drug loading efficiency

The core/shell structure of DCP-F NPs was confirmed in TEM images (Figures 1(a) and S1). DCP-F NPs had an average diameter of 161.1 ± 45.0 nm from TEM images (TEM size, Table 1), with the core diameter of 45.8 ± 13.9 nm. The latter size is similar to that of the DCP-F precursors, namely, the nanocrystals of Dox and Cur (DC, 42.1 ± 9.4 nm, Table S1). The PDA coating conferred the DC nanocrystals with black color, as shown in the right inset of Figure 1(b). Accordingly, the average hydrodynamic size of DCP-F NP was 229.8 ± 6.1 nm, around 2-fold that of DC nanocrystals (110.6 ± 2.4 nm) (Figure 1(b) and Table 1), indicating both were slightly aggregated in PBS. DCP-F NPs were greater than DCP by about 48 nm (Table S1), indicating the presence of FA-PEG layer on the NP surface increased the size (TEM size from 154.9 to 161.1 nm) and aggregation (DLS size from 181.9 to 229.8 nm) (Table S1). In line with the size change of NPs, PDA coating on the DC NPs changed the ζ-potential from −7.6 to −11.5 mV due to zwitterionic PDA with an isoelectric point of 4.0, displaying more negative charges in PBS (pH 7.4) [23]. In addition, DCP-F had relatively smaller negative ζ-potential (−9.4 mV) than that of DCP (−11.5 mV), probably because FA-PEG chain could slightly neutralize the negatively charged PDA shell (Figure 1(c), Table S1). All other NPs used in this work (Table 1) had similar characteristics (Figure S2 and Table S1).

The DCP-F NPs were examined in terms of the fed Dox/Cur mass ratio and PDA coating time (Figures S3 and 4). To enhance the photothermal effect of DCP-F, the additional PDA coating was conducted for 12 h, with the TEM diameter

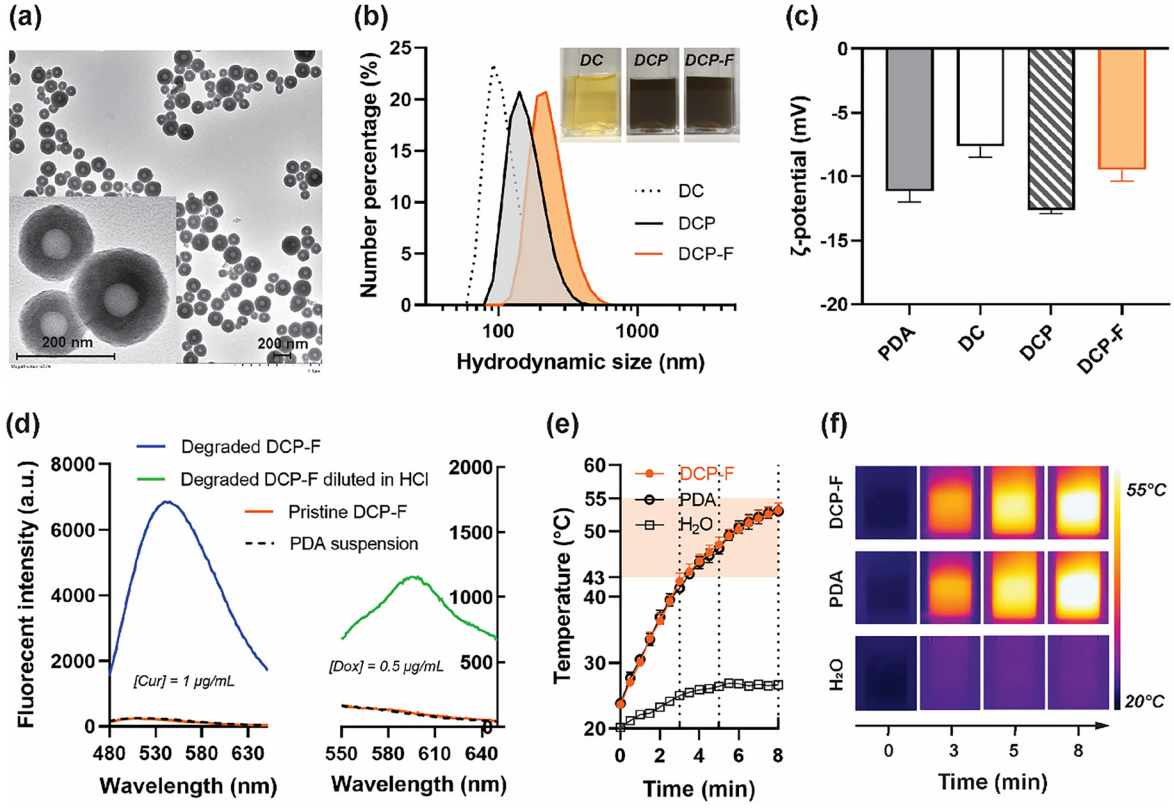

Figure 1: Physicochemical characteristics of DCP-F NPs.
(a) Representative TEM images of DCP-F NPs; (b) hydrodynamic size distribution and (c) ζ-potential of typical NPs; (d) fluorescence spectra of typical NPs upon excitation at 433 nm (left) and 490 nm (right), respectively; (e) temperature profiles (f) and thermal images of DCP-F suspensions upon 808 nm laser irradiation at 1 W/cm^2 within 8 min.

Table 1: Basic physicochemical properties of NPs prepared in this work.

NP	Modality	TEM Size (nm)	DLS size (nm) and PDI			ζ-potential (mV)
			Number mean	Z-average	PDI	
P-F	PTT	130.8 ± 1.9	160.9 ± 3.6	179.5 ± 2.4	0.032 ± 0.010	−10.7 ± 1.9
DP-F	Dox, PTT	176.9 ± 3.2	200.0 ± 17.3	240.1 ± 24.2	0.199 ± 0.031	−10.6 ± 1.0
CP-F	Cur, PTT	181.1 ± 3.2	206.0 ± 7.2	283.6 ± 1.7	0.202 ± 0.008	−9.5 ± 0.5
DCP-F	Dox/Cur, PTT	161.1 ± 4.1	229.8 ± 6.1	265.9 ± 4.3	0.116 ± 0.020	−9.4 ± 1.5

D, C, P, and F are denoted as doxorubicin, curcumin, polydopamine, and folic acid, respectively.

increasing from 142.2 to 154.9 nm (Table S2), which increased the absorption at 808 nm by 6.2 times (Figure S4b). The loading efficiencies (LEs) of Dox and Cur reached as high as 62.0 and 73.3%, respectively, with increasing fed Dox/Cur mass ratios (Figure S3c). For the final DCP-F NPs used in this work, the LEs of Dox and Cur were 56.4 ± 6.1% and 73.5 ± 6.8%, respectively, at the fed Dox/Cur mass ratio of 0.075. Accordingly, the weight percentage of PDA, Cur, and Dox in DCP-F NPs were around 85.1, 14.2, and 0.7%, respectively, i.e. the mass ratio of PDA:Cur:Dox was nearly 60:10:0.5. The major reasons for such an efficient drug loading in DCP-F NPs include (1) hydrogen bonding among the amine/imine groups of Dox and the hydroxyl groups, the α,β-unsaturated carbonyl groups in Cur [24], and the phenolic hydroxyl groups of PDA [25]; (2) electrostatic interactions between negative Cur (pKa_1 = 7.8) and positive Dox (pKa = 8.2) [26, 27]; (3) supramolecular π−π stacking between aromatic components in Dox/Cur and PDA [28, 29]; and (4) hydrophobic forces among Cur and Dox molecules [9, 30].

Note that the Tyndall effect was typically observed in DCP-F suspension (H_2O). This effect disappeared once DCP-F NPs were redispersed by DMSO, along with yellow color appearing (Figure S5c), indicating the hydrophobic

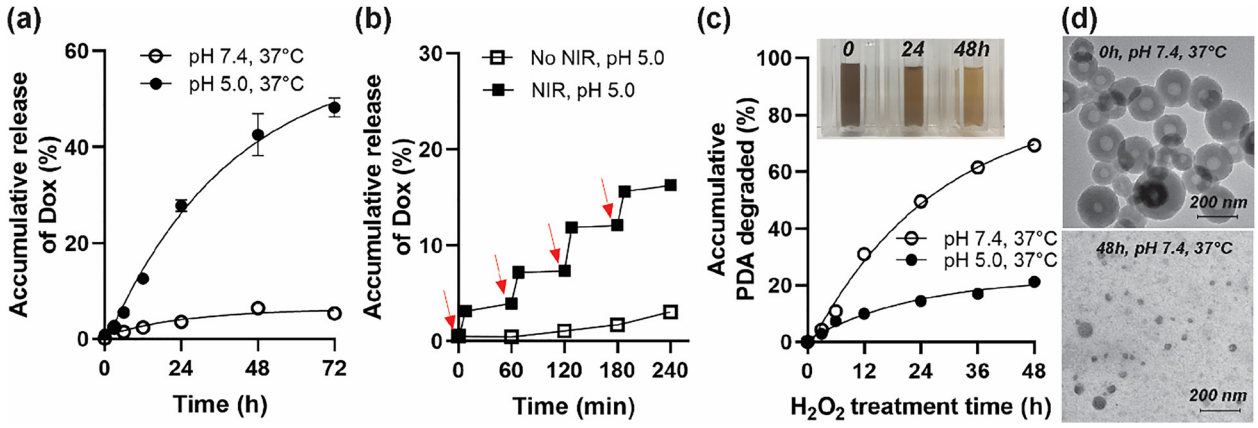

Figure 2: Release characteristics of DCP-F NPs.
Dox release profile in response to (a) pH and (b) NIR irradiation (1 W/cm^2, 8 min) at room temperature; (c) degradation, and (d) TEM images of PDA in 10 mM H_2O_2 at pH 7.4 and 5.0, respectively.

Cur/Dox cores were dissolved in DMSO. The TEM images of DCP-F dissolved in DMSO further demonstrate that DCP-F NPs were completely degraded into small debris after 2 h (Figure S5a-b). Further, the fluorescence of such DCP-F dissolution was examined to determine the presence of Cur and Dox. As shown in Figure 1(d), the maximum emission of Cur at 542 nm in the DCP-F dissolution was markedly increased upon excitation at 433 nm in comparison with DCP-F NP suspension (H_2O). A similar fluorescence phenomenon was observed at the maximum emission of Dox (595 nm) upon excitation at 490 nm using the DCP-F dissolution 10× diluted by HCl (pH 2). These marked change in the fluorescence between intact DCP-F and dissolved one demonstrated that Cur and Dox were well encapsulated inside DCP-F NPs and as a result, their instinct fluorescence was quenched by the PDA shell as well as each other owning to their selfassembly [29].

Moreover, the photothermal conversion capability of DCP-F NPs was demonstrated upon 808 nm laser irradiation at 1 W/cm^2, as shown in Figure 1(e) and (f). DCP-F NPs at the equivalent PDA concentration of 60 μg/mL raised the environment temperature from 23 °C to 53 °C in 8 min, the same as pure PDA nanoparticles, but much greater than that (~26 °C) of deionized water.

NH_2-PEG-FA conjugates were used to modify DCP via Schiff/Michael reaction between the amine group in NH_2-PEG-FA and the catechol/quinine group on the PDA sell [29]. As shown in Figure S6a, two characteristic absorptions of PEG, i.e. the band at 2868 cm^{-1} for the asymmetric stretching vibration of $-CH_2$ and the band at 960 cm^{-1} for stretching vibration of –C–O–, were also observed in the spectrum of DCP-F. The characteristic band of FA at 764 cm^{-1}, corresponding to the N–H wagging vibration of amine [31] and broadening bands at 1510 and 1580 cm^{-1} attributed to vibrations of –COO– groups were also observed in the spectrum of DCP-F NPs. Therefore, DCP-F NPs were successfully functionalized with FA via PEG linkage. Such FA-PEG-modified DCP-F NPs were colloidally stable in PBS, DMEM (10% FBS), and 50% FBS for 48 h, as the DLS particle size was not changed (Figure S6b).

3.2 On-demand drug release in response to pH, NIR, and ROS

Dox release was enhanced at pH 5.0, with up to ~40% of loaded Dox released within 48 h, whereas only 6.4% released at pH 7.4 (Figure 2(a)), indicating that acidic intracellular compartments (such as endosome and lysosome) would accelerate Dox release during the DCP-F internalization. As discussed previously, the driving forces for loading Dox could be attenuated in acidic buffer and particularly the protonated amino group of Dox increases Dox solubility [27, 29], leading to a faster Dox release in pH 5.0 buffer. Moreover, the heating generated from NIR irradiation jump-started Dox release (Figure 2(b)), where approximately 16.2% Dox released within 4 cycles of NIR heating treatments in comparison with that (3.1%) released only in pH 5.0 buffer within 4 h. This burst heat-triggered release suggests that the Dox release can be enhanced via remote NIR treatment in an on-demand manner.

Interestingly, Cur release was enhanced in the presence of DOPA phospholipid (200 μg/mL) at pH 5.0, with up to 50% of loaded Cur released within 48 h, in sharp contrast with only 10% released in the absence of the lipid (Figure S8a). This lipid-enhanced solubility of Cur may imply that the abundant lipid contents in the intracellular membrane would favor Cur release during the transport of

DCP-F between various intracellular compartments given lipophilic Cur has a high LogP (~4.0) [9]. Moreover, the acidic condition slightly enhanced Cur release (Figure S8a), as for Dox release, which can be attributed to the attenuated electrostatic forces between PDA and Cur given that zwitterionic PDA has an isoelectric point of 4.0 [23] and Cur has no protonated group in acidic solution [9]. Further note that H_2O_2 could degrade the PDA shell of DCP-F NPs in a time-dependent manner (Figure 2(c)), which enhanced the Cur release. The typical black color of DCP-F NP suspension was gradually bleached within 48 h and the typical core/shell structure collapsed as shown in the upper inset photograph (Figure 2(c)) and TEM images (Figure 2(d)). Reversely, the degradation was quicker in the neutral condition, i.e. 69.4% at pH 7.4 versus 21.3% at pH 5.0 (Figure 2(c)), which is attributed to oxidation of more perhydroxyl anions with H_2O_2 in pH 7.4 buffer [32]. Our observation is consistent with other research using plant polyphenols, which are PDA analogues [33, 34]. Therefore, the Cur release would be also promoted in the intracellular environment particularly in the neutral cytoplasm where there is a high level of H_2O_2 in colon cancer cells [35]. Taken together, Dox/Cur in DCP-F can be triggered to release in the tumor tissues all the way from the acidic TME (Dox) and intercellular phospholipid-bound compartments (Cur) to the neutral H_2O_2-rich cytosol.

3.3 Targeted cellular delivery and PTT-enhanced cytotoxicity

The cellular uptake of as-prepared DCP-F NPs was examined via determining the amount of intracellular Cur using CP-F as a simplified model to exclude the possible fluorescence interference from Dox given CP-F and DCP-F had the same surface chemistry as they were both coated with FA. As shown in Figure 3(a), cells took up CP NPs a few times that of free Cur at the same Cur dose, indicating the facilitation of PDA NPs to Cur cellular uptake. Moreover, FA-modified CP-F NPs further enhanced the cellular uptake by 80% compared with the nontargeted CP NPs, due to the overexpression of FA receptors on the colon cancer cell surface [36, 37]. Complementarily, FA inhibition assay corroborated the FA-mediated cellular uptake. Thus, as-prepared FA-modified DCP-F NPs would have high cellular uptake, similarly to CP-F NPs, by specifically targeting the overexpressed FA receptors on the cancer cell surface.

PDA was found to have negligible toxicity to cancer cells using P-F NPs as the model NPs at up to 120 μg/mL (Figure S9a), but P-F NPs showed a dose-dependent cytotoxicity upon 808 nm irradiation at 1 W/cm^2 for 8 min. Similarly, the dose-dependent cytotoxicity was observed for DP-F (Dox) and CP-F (Cur) NPs, in line with the higher cellular uptake (Figure 3(a)) and toxicity of Dox and Cur. In general, these FA-modified NPs displayed more potent inhibition than their counterparts without FA (i.e. DP and P NPs, Figure S9a-b). Note that there was no clearly enhanced cytotoxicity of FA modification in CP-F NPs compared with CP NPs, probably because (1) FA-enhanced Cur uptake just causes the marginal effect on cytotoxicity due to its high IC_{50} (18.6 μg/mL); (2) the slow release profile (Figure S8a) and the ROS-susceptivity of Cur compromises the toxicity of free Cur inside cells. Based on these dose-dependent responses, the dose for P-F (+laser), CP-F (Cur) and DP-F (Dox) NPs that resulted in 75–80% cell viability was 60, 10, and 0.5 μg/mL, respectively, similar to their ratio of calculated IC_{50} values (107.9, 18.6, and 1.46 μg/mL, Table S3). Thus, their mass ratio (60:10:0.5 of PDA:-Cur:Dox) in DCP-F NPs was determined as the optimal formulation, and similarly prepared for the use in following *in vitro* and *in vivo* experiments.

Subsequently, the combination treatments were examined (Figure 3(b)). At 0.5 μg/mL of Dox, 10 μg/mL of Cur and 60 μg/mL of PDA, the dual chemotherapy (DCP-F without laser) caused 41.5% cell death, whereas the monotherapeutic DP-F and CP-F NPs killed 17.9 and 26.6% cancer cells, respectively, indicating a simple additive effect of Dox and Cur in the combination mode and being consistent with the comprehensive study of Cur-combined chemotherapy [38]. Markedly, NIR irradiation (8 min at 1 W/cm^2) enabled DP-F, CP-F, and DCP-F to kill 38.8, 49.3 and 85.4% cancer cells at the same doses (Figure 3(b)), with the combination index (CI) of 1.15, 1.23 and 3.38 (Table S4), respectively. Consistently, the dose-dependent PTT-enhanced cytotoxicity of DCP-F NPs was observed with markedly reduced IC_{50} values ($3.91 \pm 0.16/0.20 \pm 0.01$ vs. $10.9 \pm 0.3/0.55 \pm 0.02$ μg/mL of Cur/Dox without NIR irradiation, Figure 3(c) and Table S3), demonstrating that PTT strongly synergized the dual chemotherapy of DCP-F NPs.

The cell death via PTT-enhanced combination treatments was further characterized by examining cell membrane integrity using propidium iodide dye (PI) [20]. As shown in Figure 3(d) and (e), the PI-permeable cell percentage was increased depending on the NIR irradiation time after 24 h of PTT treatment, indicating that PTT could cause loss of plasma membrane integrity. In combination with drugs, PTT caused more loss of cell membrane integrity (Figure 3(f) and (g)). In particular, ~80% cells lost the membrane integrity in DCP-F + *L* treatment. Supportively, more smaller DNA fragments (~1.5 Kb) were detected in cells receiving PTT-combined treatments (DCP-F + *L*,

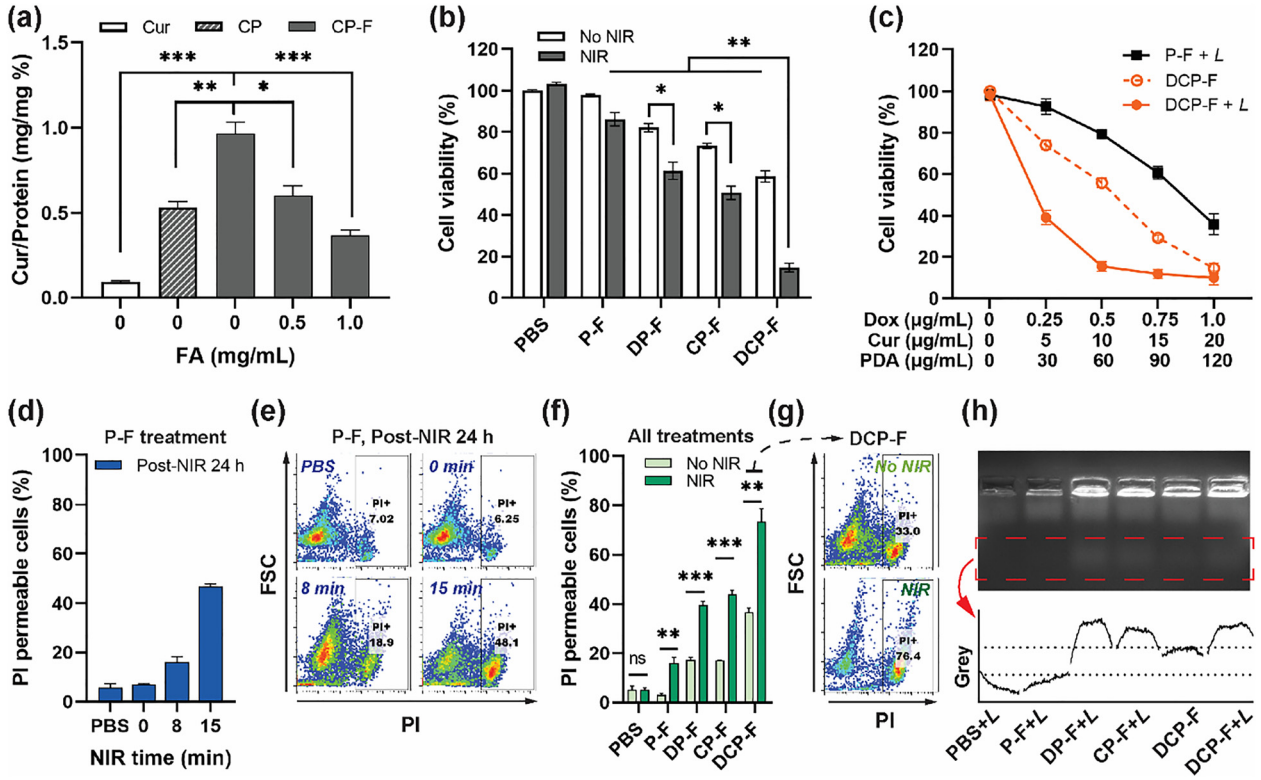

Figure 3: Cellular uptake, cytotoxicity and cell death profile.
(a) Cellular uptake of free Cur, CP and CP-F NPs in 6 h incubation; (b) cell viability upon treatments; (c) dose-dependent cell viability of PTT-enhanced dual chemotherapy; cell membrane integrity loss with P-F NPs, (d) and (e) in the time-dependent manner and (f) with different treatments; (e) and (g) the representative cytometric images; (h) gel image and the according gray density analysis of the DNA collected from culture medium after different treatments. L: denoted as NIR laser treatment, i.e. 808 nm laser irradiation at 1.0 W/cm^2 for 8 min if not specially mentioned. Cell treatment condition: 0.5, 10 and/or 60 μg/mL of Dox, Cur and/or PDA for 48 h.

DP-F + *L* and CP-F + *L*) compared with dual chemotherapy (DCP-F) (Figures 3(h) and S10). In line with cell viability data, PTT-dual chemotherapy (DCP-F + *L*) performed the best among all treatments in term of the release amount of all DNA fragments observed in the gel image (Figure S10). In summary, PTT-combined dual chemotherapy enhanced the cell death and DNA fragmentation.

3.4 Effective on-tumor photothermal conversion and complete tumor elimination

The performance of DCP-F NPs on tumor inhibition was evaluated in comparison to the other treatments, as scheduled in Figure 4(a). Prior to this, the photothermal conversion *in vivo* was conducted. At 18 h post injection of DCP-F NPs with the equivalent dosage of 30, 5 and 0.25 mg/kg for PDA, Cur, and Dox, respectively, laser irradiation at 1 W/cm^2 for 5 min heated the tumor surface up to around 50 °C, more efficient than irradiation at 0.7 and 0.5 W/cm^2 (Figure 4(b) and(c)). The temperature difference was not clearly increased along with the post-injection time (12, 18, and 24 h) (Figure S11b). Thus, laser irradiation for 5 min at 1 W/cm^2 at 18 h of post-injection was used as a tradeoff condition.

The tumor growth curve of G1 mice was used a control. Of particular note, DP-F + *L* (G2) was excluded from the inhibition evaluation because 3 mice were euthanized in the middle way in accordance with animal ethics guidelines. As shown in Figure 4(d), the tumor volume after the treatment with dual chemotherapy using DCP-F (G4) displayed 59% of tumor inhibition on day 6. Unfortunately, such inhibition did not persist and the tumor relapsed on day 8 and 10, with 36 and 42% inhibition. In sharp contrast, tumor growth in DCP-F + *L* treated group (G5) was markedly suppressed in the entire treatment course with a smaller variation of inhibition efficiency compared with other groups, with around ~92% inhibition on day 10 (Figure 4(d), (f) and (g)). These data indicate that PTT significantly enhanced the dual chemotherapy of DCP-F, without obvious tumor relapse in the end of experiments.

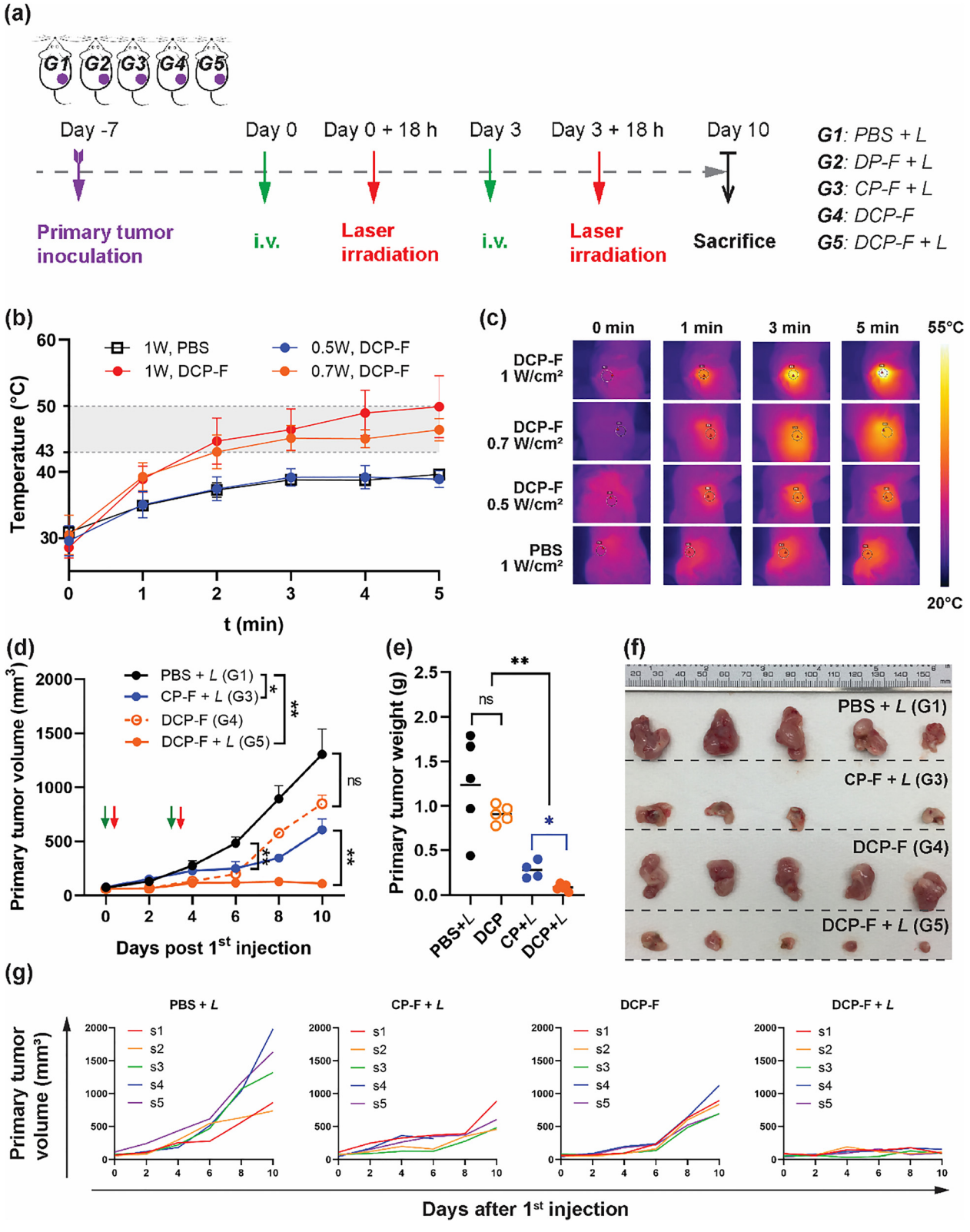

Figure 4: Primary tumor inhibition of different treatments.
(a) Tumor inoculation and treatment schedule; (b) in vivo tumor temperature and (c) representative thermal images; (d) tumor growth profile and (e) tumor weight at day 10 after 1st injection; (f) tumor photographs of each treatment group at day 10; and (g) tumor growth profile of each mouse in each group. L: denoted as NIR laser treatment, i.e. 808 nm laser irradiation for 5 min. Note that one mouse in CP-F + L (G3) was culled due to accident leg injury. Intense adaptive immune responses promoted via DCP-F + *L* treatment.

The effectiveness of PTT on enhancing chemotherapy was also corroborated by the data in CP-F + *L* (G3) group, where the PTT-combined single chemotherapy (CP-F) overtook the dual chemotherapy (DCP-F), i.e. 53 versus 42% tumor inhibition on day 10. This PTT-enhanced inhibition was validated by comparing the tumor weight on day 10 (Figure 4(e)). The tumor growth inhibition using PDA-mediated PTT alone (i.e. P-F + *L*) in the similar conditions should be weaker than or at most similar to that of CP-F + *L* (53% inhibition of tumor growth on day 10). The inhibition of P-F + *L* is further estimated to be similar to the reported (~50% inhibition at a dose of 16 mg/kg of targeting PDA NPs under 2 W/cm^2 for 5 min) [39]. In addition, the histochemical assay of tumor tissues was not conducted in this work given that the histochemical effect of PDA-based PTT, Dox [21], and Cur [40] on the tumor tissues was well characterized and summarized [21].

Therefore, PTT strongly enhanced mono- and dual-chemotherapy, in consistence with the *in vitro* cytotoxicity results.

3.5 Intense adaptive immune responses promoted via DCP-F + L treatment

The mice adaptive immune response after combined PTT and dual chemotherapy treatments was profiled on day 10 by examining the splenocyte population.

As shown in Figure 5, a similar number of $CD3^+CD8^+$ and $CD3^+CD4^+$ cells was observed in PBS + *L* (G1), DCP-F (G4) and CP-F + *L* (G3) (Figure 5(a) and (b)), which suggests adaptive immune activation did not occur in these groups. By contrast, DCP-F + *L* (G5) treatment significantly elevated the lymphocyte number, with 1.37- and 1.46-time $CD3^+CD4^+$ and $CD3^+CD8^+$ spleen T cells promoted, respectively, in comparison to G1 (Figure 5(a) and (b)). Note that the number ratio of $CD4^+/CD8^+$ T cells remained stable at around 2.0 in all treatment groups without significant change, which indicates no impaired immune system occurred in all groups after the treatment [41]. Therefore, the adaptive immunity was well built against the colon cancer, in consistence with previous reports for hyperthermia-promoted antitumor immunity via PDA-coated gold nanoparticles [11] and other nanoparticles [42, 43]. Such antitumor immunity established by DCP-F + *L* in our work can be rationally attributed to that (1) PDA-mediated PTT damages multidrug resistance proteins and causes synergistic cytotoxicity in combination with Dox and Cur [4], and as a result, such potent cytotoxicity (as shown in Figure 3(b) and (c)) forces tumor cells to succumb to immunogenic necroptosis or even necrosis rather than tolerogenic cell death such as apoptosis in the opposite way; (2) Cur enhances such Dox-induced ICD [8] to favor antitumor immune cells (Figure 5(c) and (d)); (3) PTT strengthens cell membrane integrity loss and spurs DAMPs emission such as cytosolic DNA as shown above in Figures 3(h) and S10, which can collectively stimulate the immune system with other DAMPs via particular stimulator of interferon genes (STING) pathway [44, 45]; and (4) the controllable drug release in response to acidic and ROS-rich TME and NIR (Figure 2) attenuates Dox's myelosuppression that undermines antitumor lymphocyte proliferation [2]. As such, Dox/PTT/Cur complements one another to deliver proper immunogenic signals to the immune system and augments the immunogenicity of as-developed DCP-F, as observed in our results. Taken together, DCP-F + *L* successfully combined Dox/Cur/PTT and promoted strong antitumor immune responses as designed.

In order to confirm the antitumor efficacy of the immunity spurred by DCP-F + *L*, distal tumor was inoculated on Day 11 (group 7, G7), which received the same treatment (DCP-F + *L*) in parallel as G5 did. The control

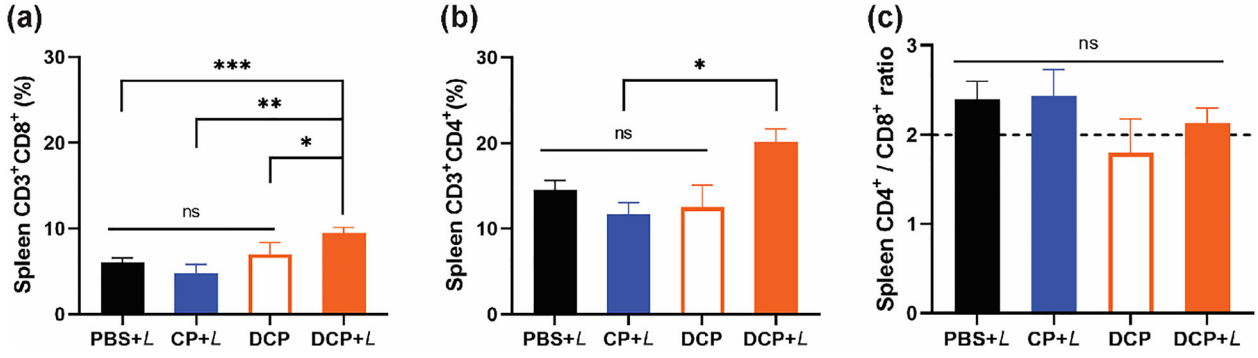

Figure 5: Peripheral adaptive immune response profile.
(a) And (b) spleen lymphocyte population and (c) the ratio of CD4 and CD8 T cells of groups G1-G5 at day 10.

group (G6) treated with PBS was inoculated with the same distal tumor, as scheduled in Figure 6(a). Encouragingly, no distal tumor growth was observed in G7 all the time whereas the distal tumor was observed in 60% mice on Day 16 and 100% mice on Day 18 in G6 (Figure 6(b)), and reached ~1400 mm^3 on day 28 (Figure 6(c)–(e), Figure S13a). These data demonstrate that the antitumor immunity stimulated by DCP-F + *L* treatment inhibited cancer challenge overwhelmingly, suggesting a great potential against cancer metastasis.

The splenocyte population and serum IgG were further examined to elucidate the underlying mechanisms. As shown in Figure 6(f) and (g), the population of $CD3^+CD4^+$ and $CD3^+CD8^+$ in group G7 was increased by 1.6 and 1.7 time compared with that of group G6 on Day 28, respectively.

Moreover, there were more IgG in group G7 that specifically binds to CT26 cells than that in group G6 on Day 28 (Figure 6(h)) based on the ELISA-like assay for the CT26-specific IgG level in serum (Figure 6(i)), suggesting the immunological memory against CT26 tumor was established after 28 days of DCP-F + *L* treatment. This result is consistent with that on the same tumor treated with the gold NP-based PTT-Dox nanomedicine [11]. Correspondingly, the primary tumor recurrence was only observed in two mice (40%) in group G7 on Day 28 (Figure S13b-c). Given that colorectal cancer cells can enter a diapause-like state to evade apoptosis from cancer treatments [46], it is plausible to assume that the residual cancer cells in the primary tumor probably survived via such a diapause-like mechanism and then maintained immunosuppressive microenvironment against the immune attacks. Such

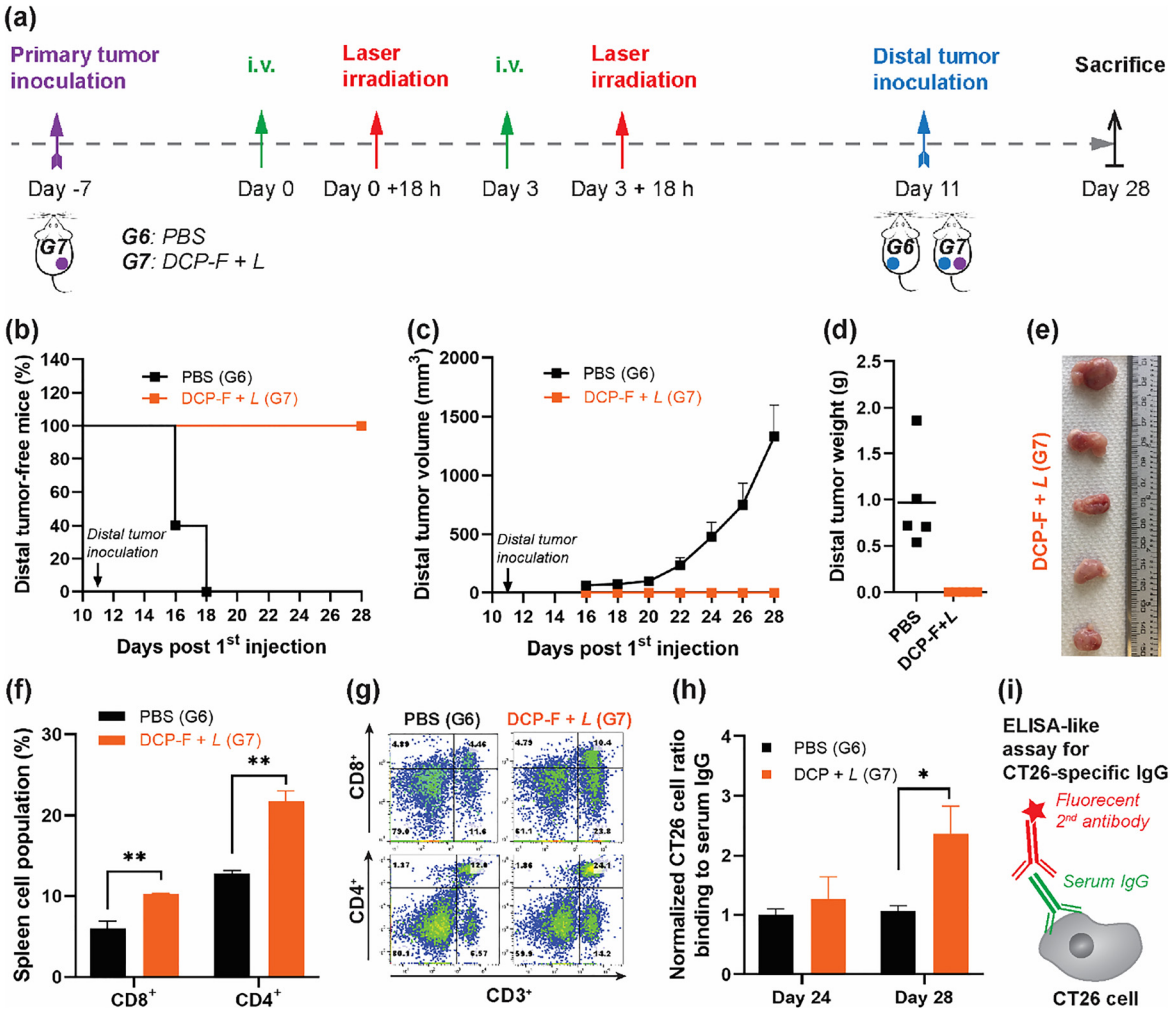

Figure 6: Tumor rechallenge after PBS and DCP-F + *L* treatments.
(a) Tumor inoculation and treatment schedule; (b) ratio of the distal tumor occurrence and (c) distal tumor growth profile after rechallenge; (d) distal tumor weight and (e) images at day 28; (f) spleen lymphocyte population and (g) representative cytometric images; (h) ratio of CT26 cells specific binding to serum IgG collected at day 24 and 28 of 1st post-injection (normalized to that before tumor inoculation); and (i) schematic of ELISA-like assay for CT26-specific IgG.

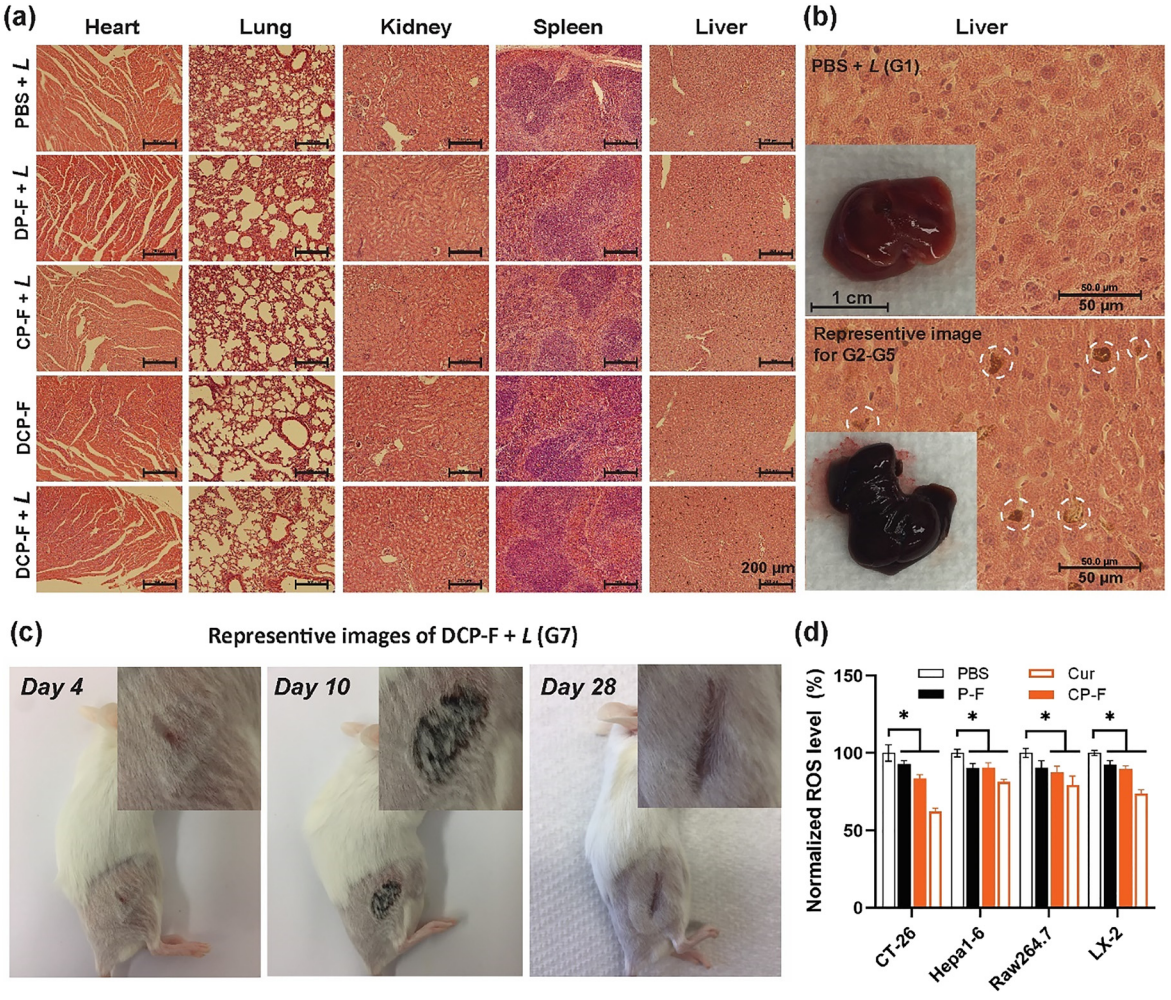

Figure 7: Safety evaluation of different treatments.
(a) and (b) H&E morphology images of major organs and (b) representative liver photographs; note that the white dashed circles indicate the black substances; (c) healing of skin injury within 28 days; and (d) intracellular ROS change of different cell lines after different treatments.

protective immunity against the distal tumor established by DCP-F + *L* in this work can be rationally attributed to that (1) the elevated $CD4^+$ T cells promote the interactions between DCs and effector T cells and the maturation of memory $CD8^+$ T cells such that a potent tumour immunosurveillance is built [47]; and (2) the development of long-lived plasma cells and memory B cells is stimulated by $CD4^+$ T cells to build protective immunity with the production of highly-selected, high-affinity antibodies other than memory $CD8^+$ cells [48]. Taken together, as-developed DCP-F NP treatment successfully built anticancer immunity with prominent inhibitory effect against primary and distal tumors, indicating great potential against tumor metastasis and relapse.

3.6 Safety evaluation

No morphological differences in major organs (i.e. heart, liver, spleen, lungs, and kidney) were observed from H&E staining results (Figure 7(a) and Figure S15) and no obvious body weight change was noted in PBS and all NP-treated groups with the equivalent total dosage of PDA, Cur, and Dox being 60, 10, and/or 0.5 mg/kg, respectively, in all formulations i.v. administered in the CT26 tumor-bearing mice (Figure S16). However, the residual NPs were observed in the liver of all NP treated groups, which may cause the aberrant black color of the liver (Figure 7(b)). Fortunately, skin injury was manifested within 6 days of two laser treatments in the form of deep-colored scars in all

laser treatment groups but completely healed on day 28 (Figure 7(c)). No health issues and death were observed in G1, G3, G4, and G5 groups, and only one mouse was culled due to accident leg injury in CP-F + *L* (G3).

Specifically, the body weight and brief necropsy report in G2 were summarized (Figure S14). Unfortunately, one mouse deceased after the second laser treatment, and two mice were culled due to deteriorating health conditions. The necropsy examination found that one mouse's stomach was empty. The mouse death and health issues in G2 could be attributed to acute inflammation, possibly caused by Dox and relatively high laser dosage rather than well-known biocompatible PDA given that (a) PDA is the primary component of the natural pigments (melanin) found in human hair and skin [49]; (b) PDA has a high median lethal dose of 483.95 mg/kg with no abnormal physiological and biochemical effect on liver [14]; and (c) the residual PDA can be metabolized by abundant biological redox mechanisms such as hydrogen peroxides (e.g. H_2O_2), an endogenous molecule produced, which widely exist in phagocytes of liver and many organs [50]. Moreover, such a clearance route of PDA via H_2O_2 was demonstrated in Figure 2(c) and (d). The well documented reports have revealed that Dox and PTT treatments cause systemic ROS-involved acute inflammation [51]. Moreover, Balb/c mice were less tolerant to cardiotoxic chemotherapeutic agents such as Dox [52–54].

Very interestingly, the ROS-scavenging activity of Cur and PDA in other three groups (G3–G5) seems to offset the acute inflammation. As shown in Figure 7(d), Cur and PDA in P-F and CP-F were observed to significantly reduce the ROS level in the normal cell lines of Raw 264.7 and LX-2, and cancer cell lines CT26 and Hepa1-6. Similarly, Figure 2(c) and (d) demonstrates the PDA component of DCP-F NPs could be depleted via H_2O_2 oxidation, which is similar to many reports that Cur attenuated acute inflammation and side effects in clinical practices [55, 56] and PDA countered oxidative damage [16–18]. Thus, Cur and PDA components in DCP-F NPs may largely offset the ROS level and maintain the mouse health in G3, G4, and G5 groups.

Taken together, the liver residual NPs and skin injury implicated that the dose of PDA, Dox, and laser irradiation should be carefully considered. These data have also provided an insight that the underlying adverse effects might be well attenuated by Cur and PDA.

4 Conclusion

We have developed a novel photochemotherapeutic delivery platform (DCP-F) for PTT-enhanced immunostimulatory/immunomodulatory dual-chemotherapy for colon cancer treatment. As-developed DCP-F nanoplatform was featured with a high loading efficiency of immunostimulatory Dox and immunomodulatory Cur. Strong tumor inhibition and satisfactory antitumor immunity were successfully achieved by delivering combined treatment modalities via the three-in-one nanoplatform. The introduction of PTT modality is not only important to strengthening the cytotoxicity of Dox and Cur but also critical to promoting the *in-situ* immunogenicity. This research work has thus provided an insight into the development of photo-chemo-immunotherapeutic nanomedicines for enhanced cancer treatment and metastasis prevention.

Acknowledgments: The authors appreciate facilities and the technical assistance from School of Biomedical Sciences (SBMS) Histology Facility of UQ and the Australian Microscopy & Microanalysis Research Facility at the Centre for Microscopy and Microanalysis (CMM). This work was performed in part at the Queensland node of the Australian National Fabrication Facility, a company established under the National Collaborative Research Infrastructure Strategy to provide nano and microfabrication facilities for Australia's researchers.

Author contributions: All the authors have accepted responsibility for the entire content of this submitted manuscript and approved submission.

Research funding: This study received financial supports from Australian Research Council (ARC) Discovery Project (DP190103486). J. Liu gratefully acknowledges the Australian Government Research Training Program Scholarship (RTP) at the University of Queensland (UQ).

Conflict of interest statement: The authors declare no conflicts of interest regarding this article.

References

[1] S. Bagchi, R. Yuan, and E. G. Engleman, "Immune checkpoint inhibitors for the treatment of cancer: clinical impact and mechanisms of response and resistance," *Annu. Rev. Pathol.*, vol. 16, pp. 223–249, 2021.

[2] L. Galluzzi, J. Humeau, A. Buque, et al., "Immunostimulation with chemotherapy in the era of immune checkpoint inhibitors," *Nat. Rev. Clin. Oncol.*, vol. 17, pp. 725–741, 2020.

[3] L. Voorwerk, M. Slagter, H. M. Horlings, et al., "Immune induction strategies in metastatic triple-negative breast cancer to enhance the sensitivity to PD-1 blockade: the TONIC trial," *Nat. Med.*, vol. 25, pp. 920–928, 2019.

[4] C. Holohan, S. Van Schaeybroeck, D. B. Longley, et al., "Cancer drug resistance: an evolving paradigm," *Nat. Rev. Canc.*, vol. 13, pp. 714–726, 2013.

[5] O. Krysko, T. L. Aaes, C. Bachert, et al., "Many faces of DAMPs in cancer therapy," *Cell Death Dis.*, vol. 4, p. e631, 2013.
[6] G. C. Jagetia and B. B. Aggarwal, "Spicing up" of the immune system by curcumin," *J. Clin. Immunol.*, vol. 27, pp. 19–35, 2007.
[7] Y. Lu, L. Miao, Y. H. Wang, et al., "Curcumin micelles remodel tumor microenvironment and enhance vaccine activity in an advanced melanoma model," *Mol. Ther.*, vol. 24, pp. 364–374, 2016.
[8] Z. Dai, J. Tang, Z. Y. Gu, et al., "Eliciting immunogenic cell death via a unitized nanoinducer," *Nano Lett.*, vol. 20, pp. 6246–6254, 2020.
[9] K. I. Priyadarsini, "The chemistry of curcumin: from extraction to therapeutic agent," *Molecules*, vol. 19, pp. 20091–20112, 2014.
[10] J. Nam, S. Son, K. S. Park, et al., "Cancer nanomedicine for combination cancer immunotherapy," *Nature Reviews Materials*, vol. 4, pp. 398–414, 2019.
[11] J. Nam, S. Son, L. J. Ochyl, et al., "Chemo-photothermal therapy combination elicits anti-tumor immunity against advanced metastatic cancer," *Nat. Commun.*, vol. 9, p. 1074, 2018.
[12] L. P. Huang, Y. N. Li, Y. N. Du, et al., "Mild photothermal therapy potentiates anti-PD-L1 treatment for immunologically cold tumors via an all-in-one and all-in-control strategy," *Nat. Commun.*, vol. 10, p. 4871, 2019.
[13] Y. Li, L. H. He, H. Q. Dong, et al., "Fever-inspired immunotherapy based on photothermal CpG nanotherapeutics: the critical role of mild heat in regulating tumor microenvironment," *Adv. Sci.*, vol. 5, p. 1700805, 2018.
[14] Y. L. Liu, K. L. Ai, J. H. Liu, et al., "Dopamine-melanin colloidal nanospheres: an efficient near-infrared photothermal therapeutic agent for *in vivo* cancer therapy," *Adv. Mater.*, vol. 25, pp. 1353–1359, 2013.
[15] K. E. Wong, S. C. Ngai, K. G. Chan, et al., "Curcumin nanoformulations for colorectal cancer: a review," *Front. Pharmacol.*, vol. 10, p. 152, 2019.
[16] H. Zhao, Z. D. Zeng, L. Liu, et al., "Polydopamine nanoparticles for the treatment of acute inflammation-induced injury," *Nanoscale*, vol. 10, pp. 6981–6991, 2018.
[17] X. F. Bao, J. H. Zhao, J. Sun, et al., "Polydopamine nanoparticles as efficient scavengers for reactive oxygen species in periodontal disease," *ACS Nano*, vol. 12, pp. 8882–8892, 2018.
[18] Y. L. Liu, K. L. Ai, X. Y. Ji, et al., "Comprehensive insights into the multi-antioxidative mechanisms of melanin nanoparticles and their application to protect brain from injury in ischemic stroke," *J. Am. Chem. Soc.*, vol. 139, pp. 856–862, 2017.
[19] K. Y. Ju, Y. Lee, S. Lee, et al., "Bioinspired polymerization of dopamine to generate melanin-like nanoparticles having an excellent free-radical-scavenging property," *Biomacromolecules*, vol. 12, pp. 625–632, 2011.
[20] W. D. Han, L. Li, S. Qiu, et al., "Shikonin circumvents cancer drug resistance by induction of a necroptotic death," *Mol. Canc. Therapeut.*, vol. 6, pp. 1641–1649, 2007.
[21] R. Mrowczynski, "Polydopamine-based multifunctional (Nano) materials for cancer therapy," *ACS Appl. Mater. Interfaces*, vol. 10, pp. 7541–7561, 2018.
[22] S. F. Yan, Q. Q. Huang, J. C. Chen, et al., "Tumor-targeting photodynamic therapy based on folate-modified polydopamine nanoparticles," *Int. J. Nanomed.*, vol. 14, pp. 6799–6812, 2019.
[23] J. Liebscher, "Chemistry of polydopamine – scope, variation, and limitation," *Eur. J. Org Chem.*, vol. 2019, pp. 4976–4994, 2019.
[24] S. Wong, J. C. Zhao, C. Cao, et al., "Just add sugar for carbohydrate induced self-assembly of curcumin," *Nat. Commun.*, vol. 10, p. 582, 2019.
[25] D. R. Dreyer, D. J. Miller, B. D. Freeman, et al., "Elucidating the structure of poly(dopamine)," *Langmuir*, vol. 28, pp. 6428–6435, 2012.
[26] K. M. Nelson, J. L. Dahlin, J. Bisson, et al., "The essential medicinal chemistry of curcumin," *J. Med. Chem.*, vol. 60, pp. 1620–1637, 2017.
[27] Y. Barenholz, "Doxil (R) – the first FDA-approved nano-drug: lessons learned," *J. Contr. Release*, vol. 160, pp. 117–134, 2012.
[28] W. R. Zhuang, Y. Wang, P. F. Cui, et al., "Applications of pi-pi stacking interactions in the design of drug-delivery systems," *J. Contr. Release*, vol. 294, pp. 311–326, 2019.
[29] Z. X. Wang, H. C. Yang, F. He, et al., "Mussel-inspired surface engineering for water-remediation materials," *Matter*, vol. 1, pp. 115–155, 2019.
[30] J. Xu, Q. H. Zhao, Y. M. Jin, et al., "High loading of hydrophilic/hydrophobic doxorubicin into polyphosphazene polymersome for breast cancer therapy," *Nanomed. Nanotechnol. Biol. Med.*, vol. 10, pp. 349–358, 2014.
[31] M. Baibarac, I. Smaranda, A. Nila, et al., "Optical properties of folic acid in phosphate buffer solutions: the influence of pH and UV irradiation on the UV-VIS absorption spectra and photoluminescence," *Sci. Rep.*, vol. 9, p. 14278, 2019.
[32] R. E. Brooks and S. B. Moore, "Alkaline hydrogen peroxide bleaching of cellulose," *Cellulose*, vol. 7, pp. 263–286, 2000.
[33] N. Young, P. Fairley, V. Mohan, et al., "A study of hydrogen peroxide chemistry and photochemistry in tea stain solution with relevance to clinical tooth whitening," *J. Dent.*, vol. 40, pp. E11–E16, 2012.
[34] E. Crastechini, C. R. G. Torres, F. A. Feitosa, C. R. Pucci, and A. B. Borges, "Influence of pH on the effectiveness of hydrogen peroxide whitening," *Operat. Dent.*, vol. 39, pp. E261–E268, 2014.
[35] S. S. Lin, Y. Y. Li, A. A. Zamyatnin, et al., "Reactive oxygen species and colorectal cancer," *J. Cell. Physiol.*, vol. 233, pp. 5119–5132, 2018.
[36] P. Kumar, P. P. Huo, and B. Liu, "Formulation strategies for folate-targeted liposomes and their biomedical applications," *Pharmaceutics*, vol. 11, pp. 381–408, 2019.
[37] P. S. Low and S. A. Kularatne, "Folate-targeted therapeutic and imaging agents for cancer," *Curr. Opin. Chem. Biol.*, vol. 13, pp. 256–262, 2009.
[38] S. H. Chen, Q. L. Liang, S. P. Xie, et al., "Curcumin based combination therapy for anti-breast cancer: from in vitro drug screening to in vivo efficacy evaluation," *Front. Chem. Sci. Eng.*, vol. 10, pp. 383–388, 2016.
[39] Y. Y. Li, C. H. Jiang, D. W. Zhang, et al., "Targeted polydopamine nanoparticles enable photoacoustic imaging guided chemo-photothermal synergistic therapy of tumor," *Acta Biomater.*, vol. 47, pp. 124–134, 2017.
[40] X. J. Yu, X. Tang, J. K. He, et al., "Polydopamine nanoparticle as a multifunctional nanocarrier for combined radiophotodynamic therapy of cancer," *Part. Part. Syst. Char.*, vol. 34, p. 1600296, 2017.
[41] J. A. P. J. Owen, S. A. Stranford, P. P. Jones, and J. Kuby, *Kuby Immunology*, 7 ed., New York, W. H. Freeman, 2013.
[42] A. S. Bear, L. C. Kennedy, J. K. Young, et al., "Elimination of metastatic melanoma using gold nanoshell-enabled

photothermal therapy and adoptive T cell transfer," *PloS One*, vol. 8, 2013, Art no. e69073.
[43] S. Toraya-Brown, M. R. Sheen, P. S. Zhang, et al., "Local hyperthermia treatment of tumors induces CD8(+) T cell-mediated resistance against distal and secondary tumors," *Nanomed. Nanotechnol. Biol. Med.*, vol. 10, pp. 1273–1285, 2014.
[44] M. Z. Lv, M. X. Chen, R. Zhang, et al., "Manganese is critical for antitumor immune responses via cGAS-STING and improves the efficacy of clinical immunotherapy," *Cell Res.*, vol. 30, pp. 966–979, 2020.
[45] L. Hou, C. Y. Tian, Y. S. Yan, et al., "Manganese-based nanoactivator optimizes cancer immunotherapy via enhancing innate immunity," *ACS Nano*, vol. 14, pp. 3927–3940, 2020.
[46] K. Sumaiyah, J. H. Rehman, and E. Collignon, "Colorectal cancer cells enter a diapause-like DTP state to survive chemotherapy," *Cell*, vol. 184, pp. 226–242, 2021.
[47] B. J. Laidlaw, J. E. Craft, and S. M. Kaech, "The multifaceted role of CD4(+) T cells in CD8(+) T cell memory," *Nat. Rev. Immunol.*, vol. 16, pp. 102–111, 2016.
[48] G. J. Yuen, E. Demissie, and S. Pillai, "B lymphocytes and cancer: a love-hate relationship," *Trends Canc.*, vol. 2, pp. 747–757, 2016.
[49] M. d'Ischia, K. Wakamatsu, F. Cicoira, et al., "Melanins and melanogenesis: from pigment cells to human health and technological applications," *Pigment Cell Melanoma Res.*, vol. 28, pp. 520–544, 2015.
[50] A. C. Cave, A. C. Brewer, A. Narayanapanicker, et al., "NADPH oxidases in cardiovascular health and disease," *Antioxidants Redox Signal.*, vol. 8, pp. 691–728, 2006.
[51] C. R. Reczek and N. S. Chandel, "The two faces of reactive oxygen species in cancer," *Annu. Rev. Cell Biol.*, vol. 1, pp. 79–98, 2017.
[52] X. J. Liu, X. G. Wang, X. Zhang, et al., "C57BL/6 mice are more appropriate than BALB/C mice in inducing dilated cardiomyopathy with short-term doxorubicin treatment," *Acta Cardiol. Sin.*, vol. 28, pp. 236–240, 2012.
[53] W. J. Aston, D. E. Hope, A. K. Nowak, et al., "A systematic investigation of the maximum tolerated dose of cytotoxic chemotherapy with and without supportive care in mice," *BMC Canc.*, vol. 17, p. 684, 2017.
[54] M. Pecoraro, A. Rodriguez-Sinovas, S. Marzocco, et al., "Cardiotoxic effects of short-term doxorubicin administration: involvement of connexin 43 in calcium impairment," *Int. J. Mol. Sci.*, vol. 18, pp. 2121–2132, 2017.
[55] T. Maulina, H. Diana, A. Cahyanto, et al., "The efficacy of curcumin in managing acute inflammation pain on the post-surgical removal of impacted third molars patients: a randomised controlled trial," *J. Oral Rehabil.*, vol. 45, pp. 677–683, 2018.
[56] Z. J. Liu, P. Y. Huang, S. K. Law, et al., "Preventive effect of curcumin against chemotherapy-induced side-effects," *Front. Pharmacol.*, vol. 9, p. 1374, 2018.

Supplementary Material: The online version of this article offers supplementary material (https://doi.org/10.1515/nanoph-2021-0202).